Rayleigh-Bénard Convection, Horizontal Convection, and Internal Gravity Waves in an experimental model of subglacial lakes

Valentine Rabaux, Louis-Alexandre Couston, Francesca Chillà, Julien Salort

Rayleigh-Bénard Convection, Horizontal Convection, and Internal Gravity Waves in an experimental model of subglacial lakes

Valentine Rabaux, Louis-Alexandre Couston, Francesca Chillà and Julien Salort

ENSL, CNRS, Université Claude Bernard, Laboratoire de physique, F-69342 Lyon, France.

(Received 3 February 2025)

We investigate experimentally the flow structure in a fluid layer heated from below and exposed to a horizontal temperature gradient on the top plate. This is a model system for the dynamics in subglacial lakes where such a competition between Rayleigh-Bénard Convection (RBC) and Horizontal Convection (HC) is thought to happen. We evidence a hysteretic transition from a RBC flow structure to a HC flow structure when the ratio of the horizontal heat flux to the vertical heat flux, Λ, is 4×10^{-4} when Λ is decreasing, and 7×10^{-4} when Λ is increasing. These values are lower than the threshold value found in recent two-dimensional Direct Numerical Simulation (DNS) (Couston *et al.* 2022), of order 10^{-2}, suggesting that HC may be more common in subglacial lakes than previously predicted. For large values of Λ, we observe that the warmest part of the top plate becomes warmer than the bottom plate, such that a stable temperature gradient settles below the warm side of the top plate. Thermal plumes are no longer visible in this region, and seem to be replaced by internal gravity waves.

Key words: turbulent convection, convection in cavities

1. Introduction

Subglacial lakes (SL) are pockets of high-pressure cold-temperature water trapped between the polar ice sheets and continental bedrocks (Siegert *et al.* 2001). They are buried under several kilometers of ice (about 2 km on average) and can be as large as Lake Michigan in the United States. To date, almost 700 subglacial lakes have been detected in Antarctica and 64 have been found in Greenland (Livingstone *et al.* 2022).

The lake geometry controls SL hydrodynamics at leading order. SL are subject to geothermal heat fluxes, on the order of 60 mW/m^2 across Antarctica (Martos *et al.* 2017) — with low heterogeneity at SL scales, which drive vertical flows whose intensity primarily depend on water depth (Couston & Siegert 2021). They are also subject to quasi-horizontal flows along the ice-water interface, when the interface is tilted and owing to the pressure-dependence of the freezing point (Thoma *et al.* 2011). These flows intensify as the interface length increases. The influence of geothermal heating (combined with depth) and interface tilt (combined with length) on SL hydrodynamics can be quantified through two key dimensionless parameters, which are the flux Rayleigh number Ra_F and horizontal Rayleigh number Ra_L, given by

$$Ra_F = \frac{g\alpha F H^4}{k\nu\kappa}, \tag{1.1}$$

$$Ra_L = \frac{g\alpha\beta\gamma L^4}{\nu\kappa}, \tag{1.2}$$

respectively. Here, L is the lake length, H is the water depth, F is the geothermal flux, g is surface gravity, α is the thermal expansion coefficient, γ is the interface slope, $\beta \approx 10^{-3}$ K/m is the rate of change of the freezing temperature with depth (linked to the pressure increase with depth), k is thermal conductivity, and ν and κ are viscosity and thermal diffusivity. The fluid properties are described by the Prandtl number $Pr = \frac{\nu}{\kappa}$, approximately $O(10)$ in SL (Couston 2021). The shape of the lake is described by the aspect ratio $\Gamma = \frac{L}{H}$. We note that most lakes can be considered fresh (Couston & Siegert 2021). The water depth, the length and the ice-water interface tilt of SL vary greatly across cases. SL can be only 10 meters deep and few hundreds of meters long, but also 1 km deep and 100s kilometers long, while the ice-water interface tilt can be close to 0 or up to few % (Couston *et al.* 2022). As a result, the range of dimensionless control parameters of interest to SL hydrodynamics research is broad, i.e. with $Ra_F \in [10^{10},\ 10^{20}]$ and $Ra_L \in [0,\ 10^{25}]$, and $\Gamma \geq 1$ (Couston & Siegert 2021).

The ratio Λ weighs the strength of the HC on RBC,

$$\Lambda = \frac{\lambda k}{F}, \tag{1.3}$$

where $\lambda = \beta\gamma$ is the temperature gradient on the top boundary. One major challenge is to determine the flow structure in the system for a given value of Λ. The numerical simulations of Couston *et al.* (2022) demonstrated a hysteretic behaviour of this model system near$\Lambda \approx 10^{-2}$ at relatively low Rayleigh numbers ($Ra_F \in \left[10^6; 10^8\right]$) and $Pr = 1$, and several aspect ratios (4, 8, 12 and 16). The range of Λ in nature is expected to be much smaller than 10^{-2}, see Table 1. Therefore, the numerical results suggest that the dynamics of subglacial lakes should be dominated by vertical, Rayleigh-Bénard like, convective motions.

This model system bears some similarity with other mixed forcing convection systems, such as the tilted heat channel (Salort *et al.* 2013; Rusaouen *et al.* 2014; Castaing *et al.* 2017), tilted Rayleigh-Bénard systems (Chillà *et al.* 2004; Zhang *et al.* 2021), and convection cells with imposed side temperature (Belmonte *et al.* 1995; Rein *et al.* 2023). In the former case, the threshold is found to be the ratio of a horizontal and vertical Rayleigh number, Ra_H and Ra_V, where in this case, it is fully defined by the cosine and the sine of the tilt angle. In our case, buoyancy is always vertical, and the vertical forcing does not have to vanish when the horizontal forcing is increased.

The objective of the work presented in this paper is to operate a simple experimental model of subglacial lakes, with $Ra_F = 10^9$ and $Pr = 7$, i.e. closer to realistic values than Couston *et al.* (2022). This flux Rayleigh number is obtained with an heating power of 100 W, corresponding to a heat-flux 2.28 kW/m^2. The Rayleigh number at $\Lambda = 0$ in this configuration is 5.4×10^7. The flow is characterized for various values of Λ, a threshold value is inferred from the change in the mean flow pattern, and a hysteretic behaviour is demonstrated.

2. Experimental setup

Our experimental setup consists in a modified RBC cell where a horizontal temperature gradient is imposed on the top boundary. The cell dimensions are $L \times H \times D = 41.5\,\text{cm} \times 6.9\,\text{cm} \times 10.5\,\text{cm}$, where L is the width, H is the height and D is the depth of the cell. The aspect ratio, $\Gamma = L/H$ is 6. The top and bottom plates are made of aluminium

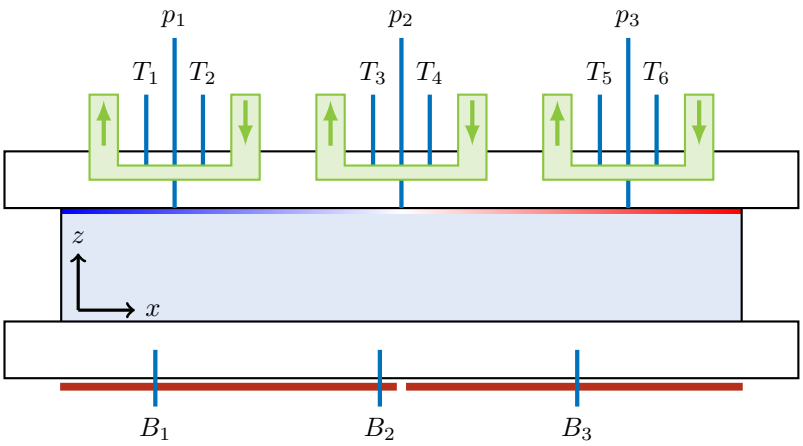

FIGURE 1. Schematic of the experimental cell. $T_1, \ldots, T_6$ are PT-100 sensors inserted into the top plate. B_1, B_2, B_3 are PT-100 sensors inserted into the bottom plate. p_1, p_2, p_3 are sensors that can be inserted into the cell to obtain temperature profiles in the bulk of the flow. The blue to red shading indicate the direction of the temperature gradient (warmer on the right).

alloy (5083) and anodized in black. The side walls are made of glass. The working fluid is deionized water at an average temperature of 20 °C ($Pr = 7$).

The heat-flux on the bottom boundary is imposed by heating with two 4 in × 8 in silicone heater mats with a maximum power of 160 W each. The top plate is cooled with three independent circulations of a mixture of water and ethylene-glycol, flowing into tight meanders machined at the top of the plate, and regulated by three independent chillers. The temperature of the plates are measured with Class 1/10 PT-100 sensors inserted into the aluminium plate: the bottom plate is fitted with three probes, and the top plate with six probes allowing to estimate the horizontal temperature gradients. A sketch of the cell is provided in figure 1.

3. Flow visualization and velocity estimates

The flow is visualized with shadowgraph with a simple diverging light optical setup, similar to that of Belkadi *et al.* (2020). The light source is a monochromatic light emitting diode at 450 nm with output power 1850 mW with an iris diaphragm to further reduce the spatial extent of the light source. For each set of control parameters, we wait for typically 24 hours, and check that all temperature values are stationary. Images are then recorded for one hour with a PCO-1600 monochrome camera with an exposure time 15 ms and a frame rate of 15 fps.

We follow the analysis of Couston *et al.* (2022), and aim to use the number of convection rolls as a proxy of the main convective mechanism: when RBC is dominant, the Large Scale Circulation (LSC) organizes in the form of several convection cells of identical size; when HC is dominant, the LSC is one large asymmetrical roll with its orientation fixed by the direction of the horizontal temperature gradient. In the latter case, there is a layer of fluid, below the warm side of the top plate, where temperature remains stably stratified. The flow organization is visible in the shadowgraph pattern, as shown in Figure 2. Note that the upwelling plumes at $x = 0$ and the downwelling plumes at $x = 41.5$ cm are not very well resolved due to light reflection very close to the walls.

In the pure RBC case ($\Lambda = 0$, bottom image), upwelling plumes are visible above the bottom plate near $x = 30$ cm, and downwelling plumes are visible below the top

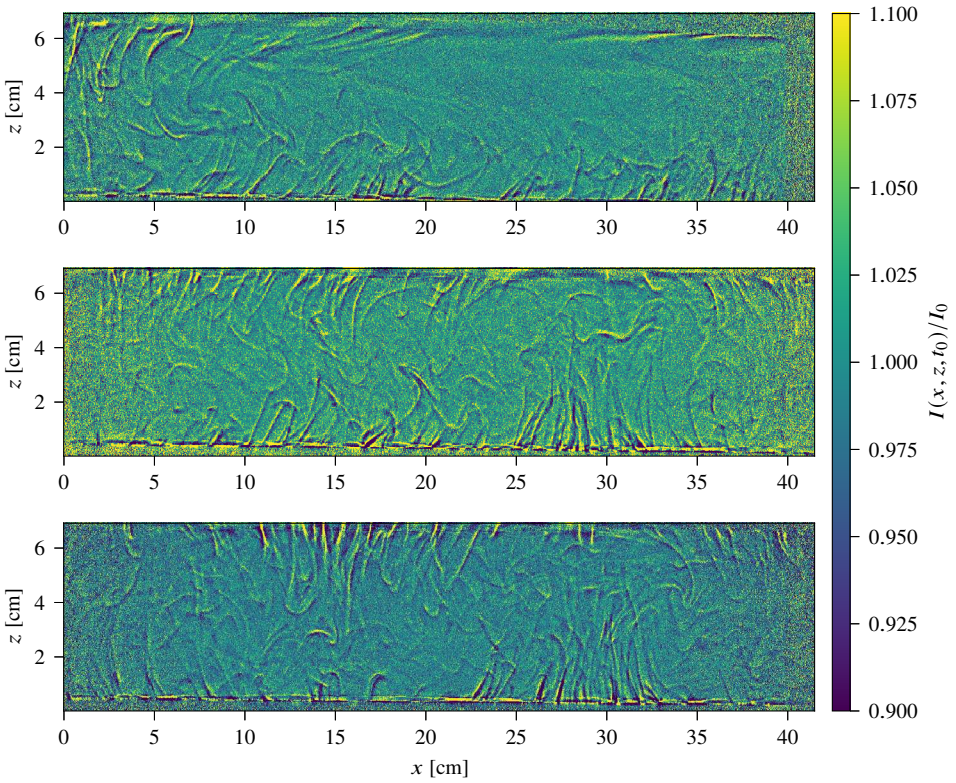

FIGURE 2. Instantaneous shadowgraph images for $Ra_F = 10^9$ and $Pr = 6.8$. The vertical temperature difference is 10 K. Bottom image: no horizontal temperature gradient (pure RBC), three convection rolls; Top image: large horizontal temperature difference (20 K across the plate width), one large roll (HC-dominated regime); Middle image: intermediate regime with a moderate horizontal temperature difference (0.6 K) showing two convection rolls.

plate near $x = 15$ cm. This corresponds to a flow structure with three convection rolls. They are not visible in the case of $\Lambda = 1.25 \times 10^{-2}$ (top image) where HC is dominant. Plumes near the bottom plate travel from left to right along the full width of the cell. Downwelling plumes are visible at $x = 0$. The asymmetry between top and bottom is clearly visible. The intermediate case ($\Lambda = 4 \times 10^{-4}$, middle image) is closer to the RBC case, with plumes observed on both plates. The upwelling plumes at $x = 27.5$ cm highlights the two convection rolls: one large roll on the left, and a smaller roll on the right. Note that the configuration with the large roll on the right, and the smaller roll on the left has also been observed in our system. In both cases, the larger roll is the one turning counter-clockwise, i.e. in the same direction as the single large roll observed in the HC-dominant case.

We derive estimates of the flow velocity from the sequence of shadowgraph images, $I(x, z, t)$, using spatio-temporal diagrams: the method is discussed in more details in previous publications (Belkadi *et al.* 2020; Méthivier *et al.* 2021). A space-time diagram is obtained by selecting an horizontal line at a given z_0, and showing $I(x, z_0, t)$ as a 2D image (see Figure 3). In this image, thermal plumes moving horizontally produce lines. The slope of the line gives the plume velocity. The lines are detected in this image with

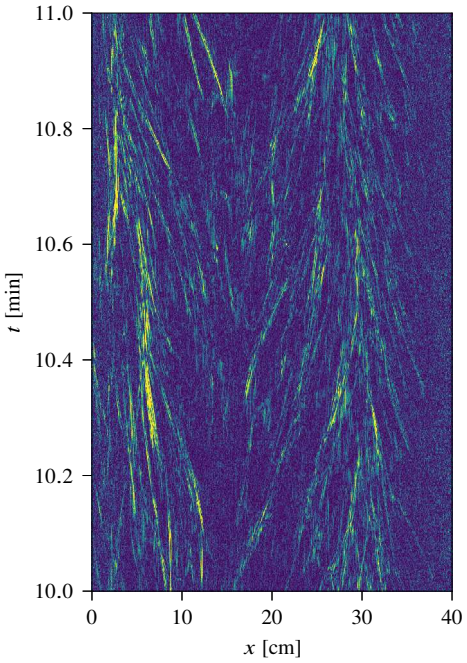

FIGURE 3. Space-time diagram obtained from the sequence of shadowgraph images for $\Lambda = 0$ at $z_0 = 5.9\,\mathrm{cm}$ (close to the top plate). Only one minute is plotted for readability.

the Line Segment Detector algorithm in the free OpenCV library (Bradski 2000), based on the algorithm of Grompone von Gioi *et al.* (2012).

Here we choose two horizontal lines, at $z_0 = 0.4\,\mathrm{cm}$ (near the bottom boundary), and $z_0 = 5.9\,\mathrm{cm}$ (near the top boundary), where the plume pattern is most visible (see Fig. 2), and plume advection yields a set of small lines at positions x_i and times t_i in the spatio-temporal diagram. The slope of each line yields an estimate of the horizontal velocity $u(x_i, z_0, t_i)$. The set of velocities can then be averaged to obtain mean profiles $\bar{u}(x, z_0)$.

Figure 4 shows the horizontal velocity profiles in the three flow regimes: they are consistent with the previously identified flow structures: RBC-dominated 3-roll large scale flow, intermediate RBC-HC 2-roll regime, and HC-dominated 1-roll regime. In the latter regime, the velocity estimates are poorly converged and vanish in the top-right part. This is because there are much fewer plumes. This is consistent with a region near the warmer side of the top boundary being stably stratified.

The analysis of the shadowgraph sequence can be carried out for several values of horizontal temperature gradient, at a given Ra_F and Pr, to determine the number of rolls as a function of Λ. The result is shown in Figure 5-a. We observe an hysteretic transition at $\Lambda_{\mathrm{decr}} = 4 \times 10^{-4}$ when Λ is decreasing, and at $\Lambda_{\mathrm{incr}} = 7 \times 10^{-4}$ when Λ is increasing. These values are much smaller than those found in the 2D DNS of Couston *et al.* (2022).

The maximum of the mean profile $\bar{u}(x, z_0)$ allows to derive an estimate for the Reynolds number,

$$Re = \frac{H\bar{u}}{\nu}, \tag{3.1}$$

shown in Figure 5-b. In this set of experiments, we observe that the horizontal temperature gradient always yields an increase in velocity: in this case, we did not see a regime

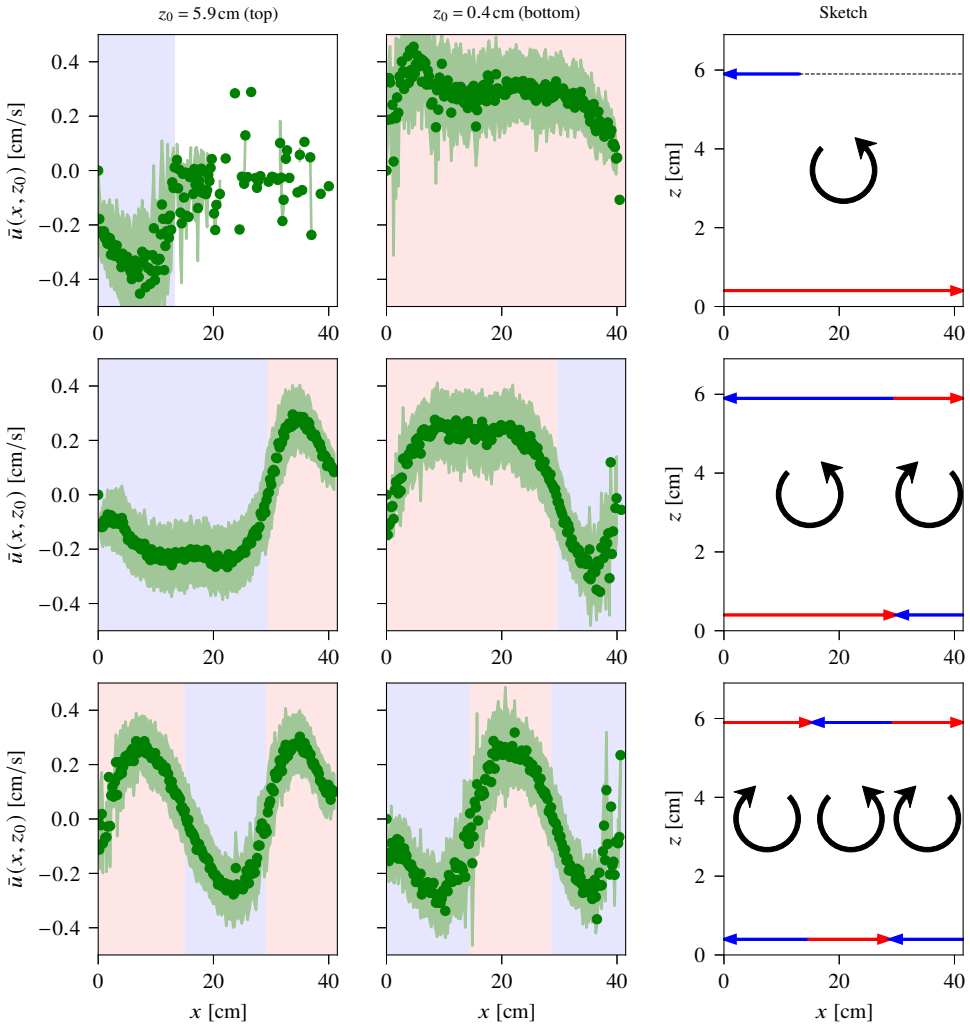

FIGURE 4. Profiles of horizontal velocity $\bar{u}(x, z_0)$, at fixed height $z_0 = 5.9\,\mathrm{cm}$ (close to the top plate), and $z_0 = 0.4\,\mathrm{cm}$ (close to the bottom plate), for $\Lambda = 0$ (bottom row), $\Lambda = 7 \times 10^{-4}$ following the upward branch of the hysteresis, see Figure 5 (middle row), and $\Lambda = 1.2 \times 10^{-2}$ (top row). The sign of the horizontal velocity is rendered as a background colour on the plot. On the right column, a sketch of the mean flow structure is shown, based on the horizontal velocity profile.

where the horizontal convection would oppose the vertical convection flow, which may have happened if the centre roll had been rotating clockwise. This could possibly be a mechanism for yet another hysteresis, but hence is not the cause of the currently observed hysteresis. The observed velocity is also hysteretic, with the velocity on the Λ-decreasing branch higher than on the Λ-increasing branch, although the difference is not big (of order 10 %), and may be close to the experimental error.

The size of the centre roll can be estimated from the velocity profiles by finding the value of x where the mean horizontal velocity is zero, i.e. where $\bar{u}(x, z_0) = 0$. The length of the roll goes from 14 cm (approximately a third of the cell width) at $\Lambda = 0$, to 41.5 cm (cell width) for $\Lambda \gg 4 \times 10^{-4}$. As is shown in Figure 5-c, and sketched in Figure 4, the

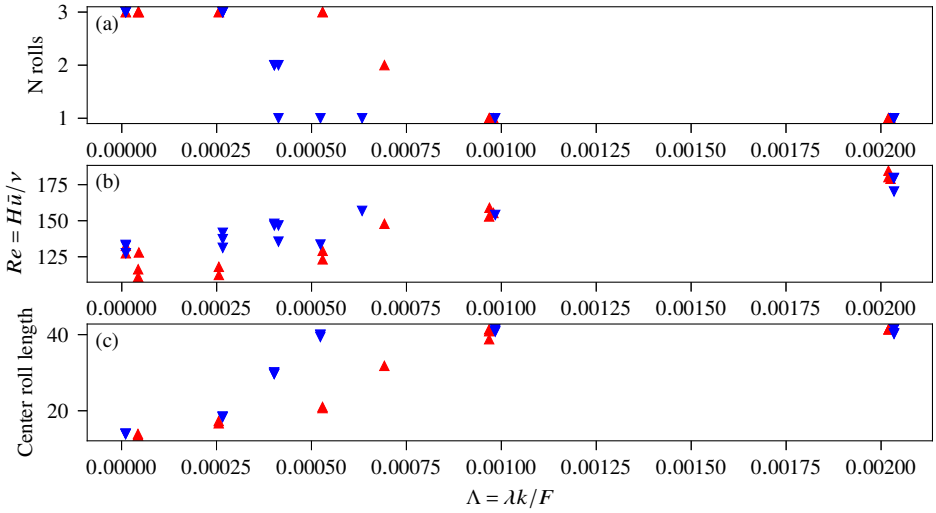

FIGURE 5. (a) Observed number of rolls, (b) Reynolds number based on the maximum of the velocity profile, and (c) width of the centre roll structure, at $Ra_F = 10^9$ and $Pr = 6.8$, for increasing (red up pointing triangles) or decreasing (blue down pointing triangles) horizontal temperature gradient, $\lambda = \Delta T_h/L$.

Lake	γ	Λ
CECs	0.016	1.63×10^{-4}
SPL	0.003	3.06×10^{-5}
Ellsworth	0.03	3.06×10^{-4}
Vostok	0.002	2.04×10^{-5}
Concordia	0.003	3.06×10^{-5}

TABLE 1. Table of the estimated slope γ, and associated Λ for the five well-known subglacial lakes discussed in (Couston & Siegert 2021; Couston *et al.* 2022), using $\lambda = 9.12 \times 10^{-4} \times \gamma$ as the estimate of the horizontal temperature gradient, $k = 0.56\,\mathrm{W/m/K}$ as the estimate for the conductivity of water, and $F = 50\,\mathrm{mW/m^2}$ as the estimate of the average geothermal flux.

centre roll continuously grows when Λ increases. At $\Lambda = 5.3 \times 10^{-4}$, its width is 20 cm but the third roll has not coalesced, so there are still 3 rolls. On the other hand, when Λ decreases from a large value, the roll size cannot decrease as long as a new roll has not appeared. We only observe a sharp decrease when a second roll has appeared. This suggests that there is a cost to change the number of rolls, and that this is the source of the hysteresis in this set of experiments. When Λ is increasing, the number of rolls will remain equal to 3 but with decreasing size of the centre roll, and increasing size of the third roll. When Λ is decreasing, Λ has to decrease further, to 4×10^{-4}, to break the unique roll into two asymmetric rolls (1/3 of the cell width for the roll on the left, 2/3 of the cell width for the roll on the right), and even further, to 2.6×10^{-4} to break the rightmost roll and recover the three rolls structure.

The expected value of Λ in subglacial lakes lies between 3×10^{-5} and 3×10^{-4} (see Table 1). The result of the DNS analysis was that $\Lambda \ll \Lambda_c \approx 10^{-2}$, therefore the lakes were expected to clearly be in the RBC regime. In this work, we find a threshold that is much closer to the Λ values in subglacial lakes. From our estimate of the critical value,

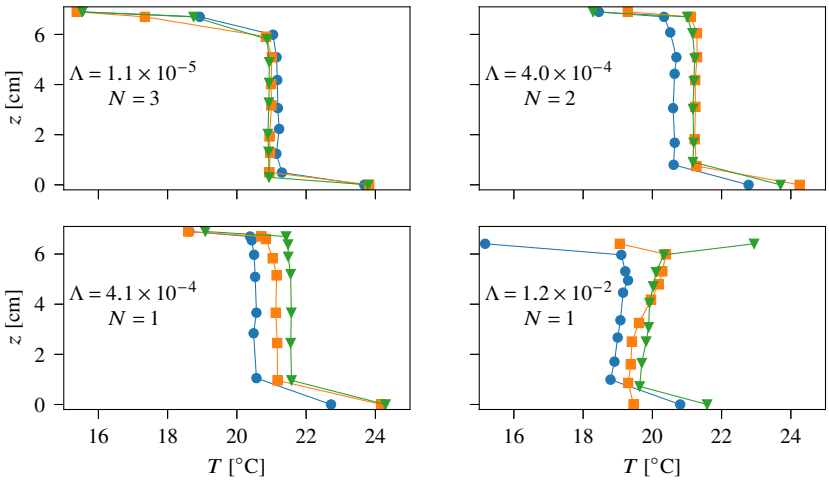

FIGURE 6. Vertical temperature profiles at $x_1 = 4.55\,\text{cm}$ (blue circles), $x_2 = 20.7\,\text{cm}$ (orange squares), and $x_3 = 36.95\,\text{cm}$ (green triangles), in the Rayleigh-Bénard-dominated regime ($\Lambda = 1.1 \times 10^{-5}$, top left), at the threshold ($\Lambda = 4.0 \times 10^{-4}$, top right), in the Horizontal Convection-dominated regime with moderate horizontal gradient ($\Lambda = 4.1 \times 10^{-4}$, bottom left), and in the Horizontal Convection-dominated regime with large horizontal gradient ($\Lambda = 1.2 \times 10^{-2}$, bottom right).

we still expect that vertical RBC-type regime will be the main driving force, but some of these lakes, particularly those with larger Λ may be in HC-type regime. Indeed, the values of Λ for the subglacial lakes are only estimates, and the critical value of Λ may also differ at these higher Pr and Ra_F values. We note that the nonlinearity of the equation of state for freshwater close to freezing may be a source of discrepancy between theoretical predictions such as drawn in this work, and flow structures in the field (Couston 2021).

4. Temperature stratification and internal gravity waves

Temperature is investigated by inserting temperature sensors inside the cell, at $x_1 = 4.55\,\text{cm}$, $x_2 = 20.7\,\text{cm}$ and $x_3 = 36.95\,\text{cm}$, shown as p_1, p_2 and p_3 in Figure 1. The probes are 2 mm-wide Class 1/3 PT-100 sensors, which can be moved along the vertical axis. The vertical position of the probes are pinpointed optically on the shadowgraph image. When they are no longer used, they are then removed from the field of view. As shown in Figure 6, each regime has a distinct signature in the temperature profiles.

At low Λ, in the Rayleigh-Bénard-dominated regime, the mean temperature is homogeneous inside the bulk: the profiles from the three probes collapse, there is no dependency with either x or z. Note that the apparent asymmetry between the top and bottom part of the profile stems from the fact that the probe can be moved inside the top plate, but cannot fully enter the boundary layer of the bottom plate. The closest it can be from the bottom plate is given by the size of the probe (4 mm).

At the threshold ($N = 2$ rolls), the temperature profiles obtained from probes 2 and 3, which are located inside the same roll, still collapse, but they differ from the profile obtained from probe 1. The temperature is still homogeneous within each roll, but the small roll on the left-hand side is colder than the large roll on the right-hand side.

At larger Λ, in the Horizontal Convection-dominated regime, the profiles no longer collapse, and a horizontal temperature gradient is visible inside the volume. For $\Lambda =$

4.1×10^{-4}, the vertical temperature gradient remains very small: even though the flow structure is heavily influenced by the horizontal temperature gradient, the mixing is still mostly similar to that of Rayleigh-Bénard. When Λ is further increased, the warmest side of the top plate becomes warmer than the bottom plate, which results in an area within the cell where the fluid is stably stratified. In this regime, thermal plumes are no longer visible on the top right part of the cell. From the temperature profile at $\Lambda = 1.2 \times 10^{-2}$, one can derive an estimate for the stable vertical temperature gradient, $\delta T/\delta z \approx 0.29\,\mathrm{K/cm}$, and therefore estimate the buoyancy frequency as (Belmonte *et al.* 1995),

$$N = \sqrt{-\frac{g}{\rho}\frac{\mathrm{d}\rho}{\mathrm{d}z}} = \sqrt{g\alpha\frac{\delta T}{\delta z}}, \tag{4.1}$$

of order $0.3\,\mathrm{rad/s}$ (or $N/(2\pi)$ of order $0.048\,\mathrm{Hz}$).

This configuration bears some similarity with systems where a stratified layer is located on top of a turbulent thermal convective layer, for example using water around its density maximum at $4\,^\circ\mathrm{C}$. In these systems, internal gravity waves in the upper layer can be generated by the eddies of the turbulent convection in the bottom layer that impinge the upper stably stratified layer (Couston *et al.* 2018; Léard *et al.* 2020). However, in these systems, the stratification is large, and the buoyancy frequency is much larger than the convective frequencies. The present case lie in the opposite regime, where the stratification is weak, and the buoyancy frequency smaller than the convective frequencies. In addition, the stratified medium is strongly sheared by the large scale circulation. However, the top right region of the cell, which is devoid of thermal plumes at large values of Λ, show some low frequency signal. In the following, we investigate this signal, and show evidence supporting the presence of internal gravity waves. Note that the existence of internal gravity waves, and their interplay with the thermal flow, is well known in the case of differentially heated cavities, where an area of stably stratified fluid settles (Patterson & Imberger 1980; Chorin *et al.* 2021; Le Quéré 2022).

The most common method for the visualization of internal gravity waves is synthetic schlieren (Dalziel *et al.* 2000), which grants access to the density gradients. This has been used extensively in salt water experiments, for example to evidence the destabilization of internal waves into secondary lower frequency waves via a triadic resonant instability (Bourget *et al.* 2013), and the destruction of background stratification in attractors through enhanced wave-induced mixing at hotspots (Scolan *et al.* 2013). In this work, we use shadowgraph instead of synthetic schlieren, because it is better suited to the visualization of thermal plumes. Indeed, thermal plumes produce strong and localised density gradients at their boundaries, while the background density in the bulk of turbulent thermal convection show much smaller fluctuations. While synthetic schlieren can be used also in this situation, and has been shown to provide useful insights (Salort *et al.* 2014), it requires a dense dot pattern and high camera resolution, or zooming on a smaller area of the convection cell.

The shadowgraph images, $I(x, z, t)$, are determined by the second derivative of the refractive index. In the limit of the small temperature fluctuations within the Boussinesq conditions, the refractive index variations are proportional to the density variations, and the density variations are proportional to the temperature variations, and the shadowgraph image can be written, at leading order,

$$\frac{I(x,z,t)}{I_0} \propto \int_0^D \left(\frac{\partial^2 T}{\partial x^2} + \frac{\partial^2 T}{\partial z^2}\right) \mathrm{d}y. \tag{4.2}$$

A monochromatic internal gravity wave, characterized by a wave vector $\mathbf{k}$ and a pulsation

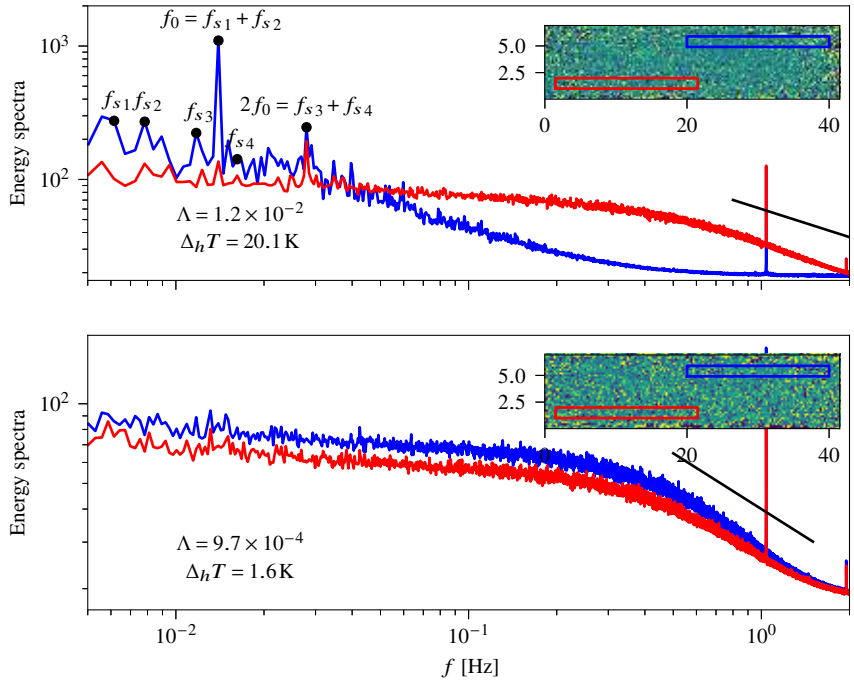

FIGURE 7. Temporal energy spectra from the shadowgraph signal, spatially averaged in the top right corner (blue lines), or in the bottom left corner (red lines). Top plot: spectra obtained in the case of a large horizontal temperature gradient ($\Lambda = 1.2 \times 10^{-2}$, top right corner devoid of thermal plumes); bottom plot: spectra obtained in the case of a smaller horizontal temperature gradient ($\Lambda = 9.7 \times 10^{-4}$, still large enough to be in HC-dominated regime, but top right corner has thermal plumes). The black lines are visual indicator of a $f^{-0.7}$ scaling law.

ω, produces a density perturbation $\delta\rho \sim \rho_0 e^{i(\mathbf{k}\cdot\mathbf{r}-\omega t)}$. The second derivative of Eq. 4.2 will conserve this spatial structure, and therefore the perturbation $\delta\rho$ should be directly visible in the shadowgraph image.

The temporal dynamics is determined experimentally by computing the Fourier transform of the shadowgraph image, $I(x, z, t)$, along the time-axis, $\hat{I}(x, z, \omega)$, and then spatially averaging its modulus squared, i.e.

$$E(\omega) = \left\langle \left| \hat{I}(x, z, \omega) \right|^2 \right\rangle_{x,z}. \tag{4.3}$$

The energy spectrum, $E(\omega)$, obtained by performing the spatial average in the top right region (plume-free at large Λ) is compared to the energy spectrum obtained by performing the spatial average in the symmetric bottom left region (Figure 7).

At moderate values of Λ (bottom plot in Figure 7), the spectrum is identical in the top-right and bottom-left regions, which shows that the temperature fluctuations have similar statistics near the top and near the bottom plate. While the horizontal temperature gradient is strong enough to change the flow structure and introduce a horizontal temperature gradient in the bulk (breaking the left-right symmetry), it is not strong enough to break the bottom-top symmetry. The spectrum is also nearly white, or slowly

decreasing, in a wide range of frequencies below $f_c \approx 0.2\,\mathrm{Hz}$. The length scale associated with this frequency is $\bar{u}/f_c \approx 1\,\mathrm{cm}$, which is close to the typical distance between thermal plumes (see Figure 2). For $f > f_c$, there is a short inertial range, where the fluctuations decrease like $f^{-\alpha}$, with $\alpha \approx 0.7$.

While the spectrum of the temperature fluctuations in the inertial range of turbulent thermal convection is usually close to $f^{-7/5}$ (Wu *et al.* 1990; Lohse & Xia 2010), the slope is found to be smaller (close to f^{-1}) for the fluctuations of the temperature gradient (Sreenivasan *et al.* 2005). For the fluctuations of the shadowgraph, it is not unreasonable that the slope could differ also, while remaining close to -1.

At large values of Λ (top plot in Figure 7), the spectrum significantly differs in the top-right region compared to the bottom left region where the dynamics are still dominated by plumes. There is much less energy in the range $f > f_c = 0.2\,\mathrm{Hz}$, and no inertial range, which shows that there is no turbulent convection, and no thermal plumes, in this region. In the bottom-left region, a spectrum close to that of turbulent convection is recovered. Additionally, the top-right region show a number of peaks at lower frequencies: one peak at $f_0 \approx 0.014\,\mathrm{Hz}$, as well as its harmonic $2f_0 \approx 0.028\,\mathrm{Hz}$. These may be waves, excited by the slower oscillations of the large scale circulation, similar to those observed by Belmonte *et al.* (1995) in the case of side-heated convection. Indeed, the large scale circulation in Rayleigh-Bénard convection exhibits slow motions on time scales much larger than that of the plumes: torsional oscillations (Funfschilling *et al.* 2008), oscillation of the wind direction (Resagk *et al.* 2006), or sloshing motion of the convection roll (Liot *et al.* 2016). These slow motions of the large scale circulation may play a similar roll in our model system as the tidal forcing in natural settings. The actual frequencies that are selected in the system will be those that match the dispersion relation for the internal waves with admissible wavenumbers.

The spectrum also shows secondary peaks, which may stem from the destabilization of these internal waves forced by the large-scale convective flow. The mechanism may be triadic resonance instability (Boury *et al.* 2023), where a wave of pulsation ω_0 gives birth to two secondary waves with lower pulsations ω_1 and ω_2, such that

$$\omega_0 = \omega_1 + \omega_2. \tag{4.4}$$

In such case, the two peaks at $f_{s1} = 6.2 \times 10^{-3}\,\mathrm{Hz}$ and $f_{s2} = 7.8 \times 10^{-3}\,\mathrm{Hz}$ are signatures of secondary waves generated by the main wave at f_0, and the two peaks at $f_{s3} = 1.2 \times 10^{-2}\,\mathrm{Hz}$ and $f_{s4} = 1.6 \times 10^{-2}\,\mathrm{Hz}$ are signatures of secondary waves generated by the main wave at $2f_0$. Interestingly, the peaks are also visible on the bottom left corner, although much weaker, which suggests that the density perturbations are advected by the wind, and have not yet dissipated when they reach the opposite side of the cell.

To characterize the spatial structure of these waves, we apply a fourth-order Butterworth bandpass filter along the time-axis of the shadowgraph images $I(x, y, t)$. As shown in Figure 8, the angle θ of the wave is quite small (less than 3°), much smaller than what would be expected by the usual dispersion relation in a quiescent fluid,

$$\omega = N \sin\theta, \tag{4.5}$$

which gives $\theta = 14°$ for $N/(2\pi) = 0.048\,\mathrm{Hz}$ and $f_{s3} = 1.2 \times 10^{-2}\,\mathrm{Hz}$. This is due to the strong horizontal velocity, which stretches the internal waves in the x direction. Indeed, the importance of the mean horizontal velocity can be assessed by the Richardson number, Ri,

$$Ri = \frac{N^2}{(\delta U/\delta z)^2}, \tag{4.6}$$

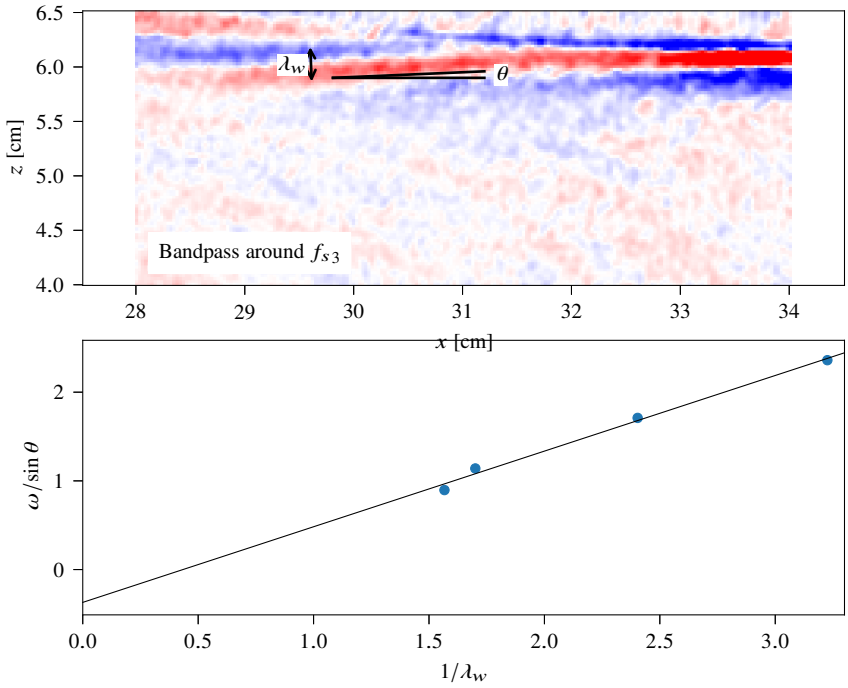

FIGURE 8. Top: example of bandpass filtered shadowgraph field, around the frequency $f_{s,3}$. The wavelength and angle of the wave near $x = 29.5\,\mathrm{cm}$ is annotated as λ_w and θ. Bottom: dispersion relation for several frequencies, at the same location ($x = 29.5\,\mathrm{cm}$). The slope of the solid line is $2\pi\bar{u}(z_0 = 6\,\mathrm{cm})$ and the ordinate at origin is $-N$ (see Eq. 4.8).

which is of order $Ri \sim 20 > \frac{1}{4}$ in our system. In this regime, the dispersion relation of internal gravity waves is given by (Booker & Bretherton 1967; Howland *et al.* 2021),

$$\omega(k_x, k_z, z) = \bar{u}(z)k_x + \frac{k_z}{\sqrt{k_x^2 + k_z^2}}, \tag{4.7}$$

which we can write as

$$\omega = \left(\frac{2\pi\bar{u}}{\lambda_w} \pm N\right)\sin\theta, \tag{4.8}$$

where λ_w is the wavelength of the wave, $\bar{u}$ is the outer horizontal flow velocity, N is the buoyancy pulsation, ω is the pulsation of the wave, and $\sin\theta$ is the angle between the wavevector of the wave and the vertical.

To verify the dispersion relation, we plot $\omega/\sin\theta$ versus $1/\lambda_w$ in Figure 8, and we find that the data is fairly compatible with Eq. 4.8. The fitting parameters yield $\bar{u} = 0.13\,\mathrm{cm/s}$ and $N = 0.37\,\mathrm{rad/s}$ (corresponding to a vertical temperature gradient $0.68\,\mathrm{K/cm}$, using Eq. 4.1). Although we do not have the resolution in either velocity or temperature profiles in this region to directly compare these values, they are not unreasonable, and fairly compatible with the temperature profile shown in Fig. 6. While the maximum horizontal velocity from Fig. 4 near the bottom plate is of order $0.2\,\mathrm{cm/s}$, the velocity near the top plate, especially this close to the plate, is expected to be lower. Therefore, the peaks

observed in the spectrum are waves, and are compatible, within experimental accuracy, to internal gravity waves with a background horizontal velocity.

5. Conclusion

In this paper, we presented an experimental realisation of a simple model of subglacial lakes. We find that the dynamics are varied and identify different regimes: pure RBC convection, mixed RBC/HC convection where the convective rolls eventually merge in a unique large roll, and HC regime, where thermal convection impinge on a stratified layer and triggers internal gravity waves, which are then advected by the Large Scale Circulation.

While the experimental investigation of this model system improves our understanding of the physics of natural systems such as subglacial lakes on Earth, or icy moons in the Solar system (Gastine & Favier 2025), it can also be seen as another way to introduce perturbations in turbulent thermal convection, and therefore ascertain the robustness of theoretical predictions to changes in flow conditions, such as the change of LSC structure in the mixed RBC/HC regime.

Acknowledgements

The authors warmly thank Marc Moulin for the design and construction of the apparatus, on particularly short notice, to keep the schedule for Valentine internship. This work benefited from the resources of the PSMN computing center in Lyon. We thank several of our colleagues in Laboratoire de physique, Julie Deleuze, Chinthaka Jacob, Sylvain Joubaud, and Philippe Odier, as well as Hélène Scolan from LMFA laboratory, for useful discussions, in particular regarding internal gravity waves; and Anne Sergent and Nathan Carbonneau from LISN laboratory for their inputs. We are also grateful to the students who are now working on the next iteration of the experiment, Valentin Chanut, Clément Bret and YuZhou Bu.

Declaration of Interests. The authors report no conflict of interest.

REFERENCES

Belkadi, M., Guislain, L., Sergent, A., Podvin, B., Chillà, F. & Salort, J. 2020 Experimental and numerical shadowgraph in turbulent Rayleigh-Bénard convection with a rough boundary: investigation of plumes. *J. Fluid Mech.* **895**, A7.

Belmonte, A., Tilgner, A. & Libchaber, A. 1995 Turbulence and internal waves in side-heated convection. *Phys. Rev. E* **51** (6), 5681.

Booker, J. R. & Bretherton, F. P. 1967 The critical layer for internal gravity waves in a shear flow. *J. Fluid Mech.* **27** (3), 513–539.

Bourget, B., Dauxois, T., Joubaud, S. & Odier, P. 2013 Experimental study of parametric subharmonic instability for internal plane waves. *J. Fluid Mech.* **723**, 1–20.

Boury, S., Maurer, P., Joubaud, S., Peacock, T. & Odier, P. 2023 Triadic resonant instability in confined and unconfined axisymmetric geometries. *J. Fluid Mech.* **957**, A20.

Bradski, G. 2000 The OpenCV Library. *Dr. Dobb's Journal of Software Tools* **25** (11), 122–125.

Castaing, B., Rusaouën, E., Salort, J. & Chillà, F. 2017 Turbulent heat transport regimes in a channel. *Phys. Rev. Fluids* **2**, 062801(R).

Chillà, F., Rastello, M., Chaumat, S. & Castaing, B. 2004 Long relaxation times and tilt sensitivity in Rayleigh-Bénard turbulence. *Eur. Phys. J. B* **40**, 223.

Chorin, P., Moreau, F. & Saury, D. 2021 Heat transfer enhancement of a natural convection flow in an enclosure submitted to a small extent thermal disturbance: Influence of location and frequency. *Int. J. Thermal Sciences* **161**, 106711.

Couston, L.-A. 2021 Turbulent convection in subglacial lakes. *J. Fluid Mech.* **915**, A31.

Couston, L.-A., Lecoanet, D., Favier, B. & Le Bars, M. 2018 The energy flux spectrum of internal waves generated by turbulent convection. *J. Fluid Mech.* **854**, R3.

Couston, L.-A., Nandaha, J. & Favier, B. 2022 Competition between Rayleigh-Bénard and horizontal convection. *J. Fluid Mech.* **947**, A13.

Couston, L.-A. & Siegert, M. 2021 Dynamic flows create potentially habitable conditions in Antartic subglacial lakes. *Sci. Adv.* **7** (8), eabc3972.

Dalziel, S. B., Hugues, G. O. & Sutherland, B. R. 2000 Whole-field density measurements by 'synthetic schlieren'. *Exp. Fluids* **28**, 322–335.

Funfschilling, Denis, Brown, Eric & Ahlers, Guenter 2008 Torsional oscillations of the large-scale circulation in turbulent Rayleigh-Bénard convection. *Journal of Fluid Mechanics* **607**, 119–139.

Gastine, T. & Favier, B. 2025 Rotating convection with a melting boundary: An application to the icy moons. *Icarus* **429**, 116441.

Grompone von Gioi, R., Jakubowicz, J., Morel, J.-M. & Randall, G. 2012 LSD: a Line Segment Detector. *Image Processing On Line* **2**, 35–55.

Howland, C. J., Taylor, J. R. & Caulfield, C. P. 2021 Shear-induced breaking of internal gravity waves. *J. Fluid Mech.* **921**, A24.

Le Quéré, P. 2022 Natural convection in air-filled differentially heated isoflux cavities: Scalings and transition to unsteadiness, a long story made short. *Int. J. Thermal Sciences* **176**, 107430.

Léard, P., Favier, B., Le Gal, P. & Le Bars, M. 2020 Coupled convection and internal gravity waves excited in water around its density maximum at 4 °C. *Phys. Rev. Fluids* **5**, 024801.

Liot, O., Gay, A., Salort, J., Bourgoin, M. & Chillà, F. 2016 Inhomogeneity and Lagrangian unsteadiness in turbulent thermal convection. *Phys. Rev. Fluids* **1**, 064406.

Livingstone, Stephen J., Li, Yan, Rutishauser, Anja, Sanderson, Rebecca J., Winter, Kate, Mikucki, Jill A., Björnsson, Helgi, Bowling, Jade S., Chu, Winnie, Dow, Christine F., Fricker, Helen A., McMillan, Malcolm, Ng, Felix S. L., Ross, Neil, Siegert, Martin J., Siegfried, Matthew & Sole, Andrew J. 2022 Subglacial lakes and their changing role in a warming climate. *Nature Reviews Earth & Environment 2022* pp. 1–19.

Lohse, D. & Xia, K.-Q. 2010 Small-scale properties of turbulent Rayleigh-Bénard convection. *Annu. Rev. Fluid Mech.* **42**, 335–364.

Martos, Y. M., Catalán, M., Jordan, T. A., Golynsky, A., Golynsky, D., Eagles, G. & Vaughan, D. G. 2017 Heat Flux Distribution of Antarctica Unveiled. *Geophysical Research Letters* **44** (22), 11,417–11,426.

Méthivier, L., Braun, R., Chillà, F. & Salort, J. 2021 Turbulent transition in Rayleigh-Bénard convection with fluorocarbon. *EPL* **136**, 10003.

Patterson, J. & Imberger, J. 1980 Unsteady natural convection in a rectangular cavity. *J. Fluid Mech.* **100**, 1.

Rein, F., Carénini, L., Fichot, F., Favier, B. & Le Bars, M. 2023 Interaction between forced and natural convection in a thin cylindrical fluid layer at low Prandtl number. *J. Fluid Mech.* **977**, A26.

Resagk, Christian, du Puits, Ronald, Thess, Andre, Dolzhansky, Felix V., Grossmann, Siegfried, Araujo, Francisco Fontenele & Lohse, Detlef 2006 Oscillations of the large scale wind in turbulent thermal convection. *Physics of Fluids* **18** (9), 095105.

Rusaouen, E., Riedinger, X., Tisserand, J.-C., Seychelles, F., Salort, J., Castaing, B. & Chillà, F. 2014 Laminar and Intermittent flow in a tilted heat pipe. *Eur. Phys. J. E* **37** (4).

Salort, J., Liot, O., Rusaouen, E., Seychelles, F., Tisserand, J.-C., Creyssels, M., Castaing, B. & Chillà, F. 2014 Thermal boundary layer near roughnesses in turbulent Rayleigh-Bénard convection: flow structure and multistability. *Phys. Fluids* **26**, 015112.

Salort, J., Riedinger, X., Rusaouen, E., Tisserand, J.-C., Seychelles, F., Castaing, B. & Chillà, F. 2013 Turbulent velocity profiles in a tilted heat pipe. *Phys. fluids* **25**, 105110.

Scolan, H., Ermanyuk, E. & Dauxois, T. 2013 Nonlinear Fate of Internal Wave Attractors. *Phys. Rev. Lett.* **110**, 234501.

Siegert, M. J., Ellis-Evans, J. C., Tranter, M., Mayer, C., Petit, J.-R., Salamatin, A. & Priscu, J. C. 2001 Physical, chemical and biological processes in Lake Vostok and other Antarctic subglacial lakes. *Nature* **414** (6), 603.

Sreenivasan, K. R., Bershadskii, A. & Niemela, J. J. 2005 Fluctuations of temperature gradients in turbulent thermal convection. *Physical Review E (Statistical, Nonlinear, and Soft Matter Physics)* **71** (3), 035302.

Thoma, M., Grosfeld, K., Mayer, C., Smith, A. M., Woodward, J. & Ross, N. 2011 The " tipping " temperature within Subglacial Lake Ellsworth , West Antarctica and its implications for lake access. *The Cryosphere* **5**, 561–567.

Wu, Xiao-Zhong, Kadanoff, Leo, Libchaber, Albert & Sano, Masaki 1990 Frequency power spectrum of temperature fluctuations in free convection. *Phys. Rev. Lett.* **64** (18), 2140–2143.

Zhang, L., Ding, G.-Y. & Xia, K.-Q. 2021 On the effective horizontal buoyancy in turbulent thermal convection generated by cell tilting. *J. Fluid Mech.* **914**, A15.